International Journal of Microwave and Wireless Technologies

cambridge.org/mrf

Interpolation of reflected and diffracted rays for accelerated ray tracing simulation

Conor Brennan[1], Allan Wainaina Mbugua[2], Yun Chen[2] and Sajjad Hussain[3]

[1]School of Electronic Engineering, Dublin City University, Ireland; [2]Huawei Technologies Deutschland GmbH, Germany and [3]School of Electrical Engineering and Computer Science, National University of Sciences and Technology, Pakistan

Research Paper

Cite this article: Brennan C, Mbugua AW, Chen Y, Hussain S (2026) Interpolation of reflected and diffracted rays for accelerated ray tracing simulation. *International Journal of Microwave and Wireless Technologies* **18**(3), 409–418. https://doi.org/10.1017/S1759078726103778

Received: 30 September 2025 UTC
Revised: 23 July 2026 UTC
Accepted: 31 July 2026 UTC

Keywords:
radio channel modeling; ray tracing; virtual drive testing

Corresponding author: Conor Brennan; Email: conor.brennan@dcu.ie

All opinions expressed are solely those of the contributing authors should not be viewed as representing the official view of Huawei.

Abstract

The efficient computation of an image-based ray trace for a receiver moving along a linear trajectory in an urban area is considered. Sampling channel information at the Nyquist rate or higher imposes a considerable computational burden, and the proposed algorithm instead utilizes the observation that such receivers will enter and exit well-defined lit regions, which define the precise extent within which reflected and diffracted rays can potentially propagate. A simple model for the associated ray is created within each lit region, obviating the need to perform an independent ray trace for each receiver location. The simple model is based on field information computed at M locations within the region. Polynomial and cubic spline interpolation is used to efficiently model amplitude and phase data along the trajectory. The paper validates the approach and demonstrates its effectiveness in the context of a simulated street-canyon environment.

Introduction

Applications enabled by emerging wireless technologies such as 5G and WiFi have led to enormous growth in recent years, with exciting use cases emerging in integrated sensing and communication and autonomous driving [1]. These technologies require high-fidelity testing and optimization, both in pre- and post-deployment, in order to meet stringent performance targets. A typical post-deployment test method in 5G and legacy communication systems is drive testing, whereby performance logs are generated and analyzed to identify potential bottlenecks. An alternative pre-deployment approach which can reduce the number of physical drive tests required is virtual drive testing (VDT) [2, 3]. Site-specific models of the radio channel are a natural tool for VDT, with ray tracing (RT) simulations being particularly attractive due to their ability to achieve good accuracy in terms of key performance indicators including pathloss, angular and delay spread [4]. RT simulations have much lower computational complexity as compared to full-wave models but, given the growing complexity of environment representations, still require significant run-times. Trade-offs between accuracy and computation times are still typically required.

In the particular case of VDT, an important observation is that neighboring frames often display coherence, that is, the set of rays arriving at the receiver (Rx) is similar. This is especially the case when the inter-frame distance is of the order of a small number of wavelengths. This has formed the basis of a number of approaches to reducing the computational burden associated with RT in the context of moving objects, specifically by either reducing the cost of constructing and validating rays, or by interpolating their associated field amplitudes. In particular, this is exploited in [5] in the context of dynamic RT in order to minimize the need to rebuild the bounding volume hierarchy and also to perform ray intersection checks, the latter being achieved by a process of propagation path caching. In [6, 7], a visibility table, defined as comprising edges and faces which are visible to the Tx and Rx, is pre-computed and used to accelerate RT simulation in urban microcellular scenarios, while in [8–10] rays identified in a single RT simulation are extrapolated based on the motion of both the interaction points and dynamic objects, allowing a dynamic RT model to be created. A major challenge in this approach is the specification of the coherence time, that is, the length of time for which the rays identified in the initial RT remain valid. Hussain and Brennan [11] outline an approach in which a well-defined geographical zone called a lit region is identified for each reflected and diffracted ray. By the laws of geometric optics and Uniform Theory of Diffraction (UTD), a valid ray can only potentially exist for receiver points lying inside this region. Combined with the complementary notion of shadow regions, this facilitates the rapid identification of points along a mobile receiver's trajectory to which reflected and diffracted rays can feasibly propagate, thereby eliminating the need for ray validation at points that are in shadow or outside the lit region. Hussain and Brennan [6] extended

© The Author(s), 2026. Published by Cambridge University Press in association with The European Microwave Association. This is an Open Access article, distributed under the terms of the Creative Commons Attribution licence (http://creativecommons.org/licenses/by/4.0), which permits unrestricted re-use, distribution and reproduction, provided the original article is properly cited.

Downloaded from https://www.cambridge.org/core. UNIVERSIDAD AUTONOMA METROPOLITANA, on 16 Nov 2026 at 02:12:28, subject to the Cambridge Core terms of use, available at https://www.cambridge.org/core/terms. https://doi.org/10.1017/S1759078726103778

this to the case of a moving transmitter, an extension which requires the efficient specification of the varying geographical extent of the lit region.

Complementary to these approaches, which attempt to reduce the burden associated with the geometrical identification of rays, is the idea of numerically interpolating their (complex-valued) field amplitudes. Linear interpolation is used in [12] to interpolate the complex amplitude of the line of sight and other multipath components. A potential shortcoming of this strategy is when it is applied to diffracted rays whose complex amplitude can vary rapidly in the vicinity of shadow boundaries. In addition, it employs simple heuristic approaches to situations where rays either appear or disappear due to shadowing along the route. A similar approach is outlined in [13] in which ray entities (i.e. collections of rays grouped by the interaction mechanism) are proposed. Interpolation of rays is identified as a potential benefit of this approach, but it is not explicitly performed.

In this paper, aspects of both approaches are combined. Firstly, lit regions in which specific rays exist are identified [11], thereby removing many cumbersome visibility and validation checks. Secondly, highly accurate (non-linear) mathematical interpolation is used to create simple models for the field amplitudes within these regions, removing the requirement to explicitly trace and process a ray to each receiver location within the region. This paper is an expanded version of [14] wherein the cubic spline interpolation models developed improve upon the simple polynomial models presented in the previous work, as they are more stable as the number of interpolation points is increased.

This paper presents an interpolation-based approach in which reflected and diffracted rays are approximated individually within their so-called lit region (defined as the region in space in which the ray can feasibly exist given the laws of geometric optics and UTD). The paper is organized as follows. Fields associated with rays vary rapidly as the Rx moves, but in Section "Ray interpolation" it is outlined how the fast-moving phase can be extracted, leaving residual fields which can be factored into several terms, each of which can be approximated accurately using interpolation. Section "Interpolation methods" introduces two interpolation approaches, polynomial interpolation and cubic spline interpolation. Section "Validation and comparison of interpolation methods" validates the method in the context of reflection and diffraction from a single building face. More complex examples involving a street canyon are presented in Section "Results." We close with conclusions and by identifying future work.

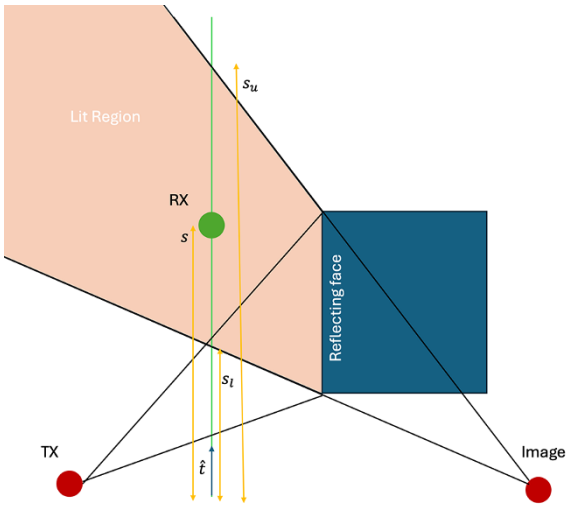


Figure 1. A receiver trajectory (green line) passing through the lit region. The reflected ray (from the reflecting face) will only exist between the shadow boundaries $s = s_l$ and $s = s_u$. Diffracted rays emanating from the edge of the reflecting face will exist along the entire route, but will exhibit discontinuities at the shadow boundaries.

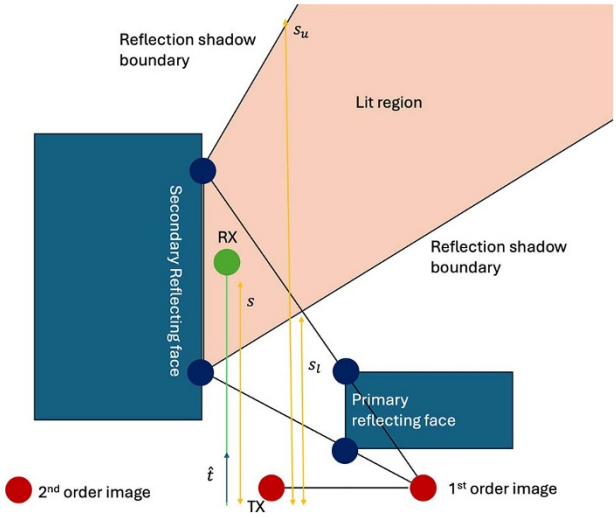


Figure 2. Construction of the lit region for a higher-order reflection.

Ray interpolation

An accurate and rapid approximation to the fields associated with a ray can be made using interpolation. The key observation in each case is that the associated field components comprise the product of a relatively slowly varying amplitude term with a rapidly varying complex exponential term. However, the phase of the latter term varies relatively slowly. The amplitude and phase terms can thus be interpolated, a process which is detailed for reflected and diffracted rays respectively in the next subsections.

Interpolation of reflected rays

Consider the situation depicted in Figure 1. A receiver is traveling on a linear trajectory (green line) in the direction $\hat{t}$. Its distance along this trajectory is given by s. It enters the lit region associated with a reflecting face at $s = s_l$, at which point it receives a reflected ray. It will continue to receive this reflected ray until it exits the lit region at $s = s_u$. The laws of geometric optics determine both s_l and s_u, while the precise definition of the lit region depends on the order of the reflection. Figure 2 illustrates its construction for second (and higher) order reflections. The electric field associated with a reflected ray is given by

$$\mathbf{E}^r(s) = \begin{bmatrix} \Gamma_\perp & 0 \\ 0 & \Gamma_\parallel \end{bmatrix} \begin{bmatrix} E^i_\perp \\ E^i_\parallel \end{bmatrix} \frac{R_1}{R_1 + R_2} e^{-\jmath k R_2}, \qquad (1)$$

where $\Gamma_\parallel, \Gamma_\perp$ are the parallel and perpendicular reflection coefficients and $E^i_\perp, E^i_\parallel$ are the perpendicular and parallel components of the incident electric field at the reflection point. R_1, R_2 are, respectively, the distances from the source to the reflection point and from the reflection point to the field point (which is located a distance s

Downloaded from https://www.cambridge.org/core. UNIVERSIDAD AUTONOMA METROPOLITANA, on 16 Nov 2026 at 02:12:28, subject to the Cambridge Core terms of use, available at https://www.cambridge.org/core/terms. https://doi.org/10.1017/S1759078726103778

along the trajectory). The complex exponential term $e^{-\jmath kR_1}$ can be factored from the incident field leaving

$$\mathbf{E}^r(s) = \mathbf{A}(s)e^{-\jmath k\hat{R}(s)} \tag{2}$$

$$= \begin{bmatrix} A_\perp(s) \\ A_\parallel(s) \end{bmatrix} e^{-\jmath k\hat{R}(s)}, \tag{3}$$

where

$$A_\perp(s) = \Gamma_\perp \left|E^i_\perp\right| e^{\jmath\phi_\perp} \frac{R_1}{R_1+R_2} \tag{4}$$

$$A_\parallel(s) = \Gamma_\parallel \left|E^i_\parallel\right| e^{\jmath\phi_\parallel} \frac{R_1}{R_1+R_2} \tag{5}$$

$$\hat{R}(s) = k\left(R_1+R_2\right). \tag{6}$$

$\phi_\perp$ and $\phi_\parallel$ are slowly varying residual phase terms which remain after the rapidly varying phase terms $k(R_1+R_2)$ are grouped together as $\hat{R}(s)$. The term $\hat{R}(s)$ (which is the total electrical length traveled by the reflected ray) varies slowly along the trajectory (although the complex exponential in Equation (2) for which it is the argument varies rapidly). Slow variations in spreading loss, reflection coefficient, antenna pattern, etc. are captured in $A_\perp(s)$ and $A_\parallel(s)$. All three slowly varying terms ($A_\perp(s), A_\parallel(s)$, and $\hat{R}(s)$) can be approximated using either low-order polynomials or cubic splines as outlined in Section "Interpolation methods."

Interpolation of diffracted rays

The presence of the optical shadow boundaries, across which the diffracted fields are discontinuous (thereby compensating for the discontinuities in the geometric optics field), complicates the interpolation process for the fields associated with diffracted rays. In particular, smooth polynomials or cubic splines will not be able to model such a discontinuity. Instead, separate interpolation models are used for portions of receiver trajectory lying between each shadow boundary. Consider the case of diffraction from the south-west corner of the building in Figure 1. One interpolation model is created for field points between $s = 0$ and the reflection shadow boundary at $s = s_l$, and another model is created for points from $s = s_l$ onwards. A similar process is applied to diffraction from the north-west corner.

A field point located a distance s along the trajectory will receive a diffracted ray from one of the edges with electric field [15]

$$\mathbf{E}^d(s) = \begin{bmatrix} E^d_{\beta_0}(s) \\ E^d_\phi(s) \end{bmatrix} \tag{7}$$

$$= \mathbf{B}(s)e^{-\jmath kR_2}, \tag{8}$$

where the term $e^{-\jmath kR_2}$ accounts for the phase acquired in free-space propagation to the field point from the diffraction point and

$$\mathbf{B}(s) = \begin{bmatrix} D_s & 0 \\ 0 & D_h \end{bmatrix} \begin{bmatrix} E^{inc}_{\beta'_0} \\ E^{inc}_{\phi'} \end{bmatrix} G(R_1,R_2) \tag{9}$$

$$= \begin{bmatrix} B_{\beta_0}(s) \\ B_\phi(s) \end{bmatrix}. \tag{10}$$

D_h and D_s are the hard and soft diffraction coefficients, while $E^{inc}_{\beta'_0}$ and $E^{inc}_{\phi'}$ are the components of the incident field at the diffraction point, using an edge-based coordinate system, and the spreading term is given by $G(R_1,R_2)$. β_0 and ϕ are angles which define the local coordinate system. More details of the derivation of these terms are available in [15].

Factoring B into amplitude and complex exponential terms yields

$$B_{\beta_0}(s) = \left|B_{\beta_0}(s)\right| e^{\jmath\theta_1(s)} \tag{11}$$

$$B_\phi(s) = \left|B_\phi(s)\right| e^{\jmath\theta_2(s)}, \tag{12}$$

where $\left|B_{\beta_0}(s)\right|, \left|B_\phi(s)\right|, \theta_1(s), \theta_2(s)$, and $R_2(s)$ are slowly varying quantities with respect to receiver motion and can thus be interpolated as per the techniques described in the next section.

Interpolation methods

The previous section outlined how the fields can be simply written in terms of a number of quantities that vary slowly with receiver motion and are thus amenable to approximation by interpolation. Two interpolation schemes are considered and compared in this paper: polynomial interpolation and cubic spline interpolation.

Polynomial interpolation

Assuming that the function to be approximated is f, interpolation proceeds by sampling the function at discrete inputs s_i, producing corresponding outputs f_i. Given $M+1$ data points of the form (s_i, f_i) for $i = 0 \ldots M$, polynomial interpolation fits a polynomial of order M

$$p(s) = a_0 + a_1 s + a_2 s^2 + \cdots + a_M s^M \tag{13}$$

where the coefficients satisfy

$$\begin{bmatrix} 1 & s_0 & s_0^2 \ldots s_0^M \\ 1 & s_1 & s_1^2 \ldots s_1^M \\ \vdots & \vdots & \vdots \quad \vdots \\ 1 & s_M & s_M^2 \ldots s_M^M \end{bmatrix} \begin{bmatrix} a_0 \\ a_1 \\ \vdots \\ a_M \end{bmatrix} = \begin{bmatrix} f_0 \\ f_1 \\ \vdots \\ f_M \end{bmatrix}. \tag{14}$$

Specification of the coefficients a_m for $m = 0 \ldots M$ thus requires field data at $M+1$ points in the lit region, obtained using exact RT to these points. Once the coefficients have been specified, they can be used to rapidly compute the reflected or diffracted fields at *any* point within the lit region as per Equations (2) and (8).

Cubic spline interpolation

A known problem with polynomial interpolation is its lack of stability when the number of data points grows, caused by the rapid variations associated with the higher-order terms (e.g. s^M) as M grows. While the polynomial is guaranteed to pass through the particular data points used to compute the coefficients, large oscillations can nonetheless develop at intermediate points. A commonly used alternative, with a similar computational cost, is cubic spline interpolation. Referring to Figure 3, we see that $M+1$ data points can be used to either fit a single polynomial of degree M through all points or a sequence of cubic polynomials over each of M subdomains where the i^{th} subdomain spans $s \in [s_i, s_{i+1}]$. The cubic polynomial (referred to as "splines") in sub-domain i is given by

$$p_i(s) = a_0 + a_1 s + a_2 s^2 + a_3 s^3 \tag{15}$$

where the four coefficients a_0, a_1, a_2, and a_3 must be computed for each sub-domain. This is achieved by fitting $p_i(s)$ to the data points

Downloaded from https://www.cambridge.org/core. UNIVERSIDAD AUTONOMA METROPOLITANA, on 16 Nov 2026 at 02:12:28, subject to the Cambridge Core terms of use, available at https://www.cambridge.org/core/terms. https://doi.org/10.1017/S1759078726103778

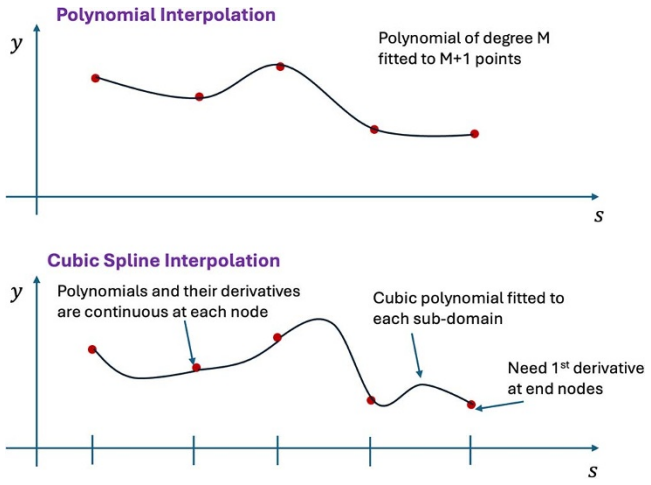


Figure 3. Polynomial and cubic spline interpolation defined on $M+1$ data points.

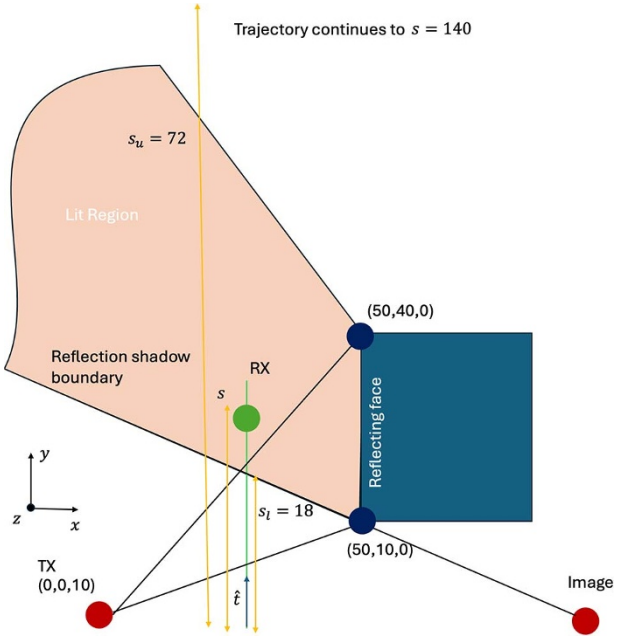


Figure 4. Geometry for validation example. Receiver travels from $s=0$ to $s=140$, passing through shadow boundaries at $s=18$ and $s=72$ as it does so.

(s_i, f_i) and (s_{i+1}, f_{i+1}). In addition, splines in adjacent sub-domains are constrained to have continuous first and second derivatives at their common vertices. These constraints yield $2M+2\,(M-1) = 4M-2$ equations. Given that a total of $4M$ coefficients are required, it is necessary to impose two further constraints. These take the form of specifying the function derivative at the end points, that is, requiring $p_0'(s_0) = \eta_1$ and $p_{M-1}'(s_M) = \eta_2$ for some boundary values η_1 and η_2. Cubic splines can be fit to a lit region by sampling M points within the lit region, performing ray traces to obtain field information at each of the M points and supplementing this with two extra ray traces at points very close to the start and end points of the lit region in order to numerically estimate the required derivative information at the boundaries.

Validation and comparison of interpolation methods

The model is validated by considering the example depicted in Figure 4.

A vertical dipole is located at $(0, 0, 10)$ and radiates at 300 MHz. A rectangular building of height 40 m, and $\epsilon_r = 4$ is located with the south-west corner at $(50, 10, 0)$. A receiver moves along a trajectory $(x = 10, y \in (0, 140), z = 10)$ as shown, and single reflections and diffractions are considered from the leftmost face of the building. The receiver crosses reflection shadow boundaries at $s = 18$ and $s = 72$, and a reflected ray therefore exists for $s \in [18, 72]$. As a reference, exact RT is used to compute the fields along a fine grid of 1200 points along the trajectory. To create the interpolated model of the reflected rays, an exact ray trace was performed at M points through the lit region, and polynomial and spline approximations were created for the slowly varying quantities as outlined in Section "Interpolation of reflected rays." A similar process was followed to create polynomial and spline interpolated models for the diffracted field. Equations (2) and (8) along with the interpolation models were used to approximate the electric fields along the same fine grid of points for which reference results were computed. The number of interpolation points, M, was varied in order to gauge how the interpolation accuracy is affected by the order of interpolation. For the case of reflected fields, interpolation was used in the lit region from $s = 18$ to $s = 72$. As outlined in Section "Interpolation methods," data at M interpolation points can be used to make a single polynomial of degree $M-1$ throughout the region or a cubic spline interpolation across each of $M-1$ subregions. In both cases, an exact ray trace is required for each of the M interpolation points. In the case of cubic spline interpolation, a further two ray traces are required, one at the start and end of the interpolation region, in order to numerically estimate the derivative of the slowly varying field quantities at these end points. In order to gauge the accuracy of both the magnitude and phase of the fields, we examine the behavior of the real components of the field throughout the region. At each of the $N = 1200$ points in the lit region, we compute the error as

$$\epsilon(\vec{r}) = \left|\Re\{E_z(\vec{r})\} - \Re\{\tilde{E}_z(\vec{r})\}\right| \tag{16}$$

where E_z is the exact z component of the electric field while $\tilde{E}_z$ is the interpolated approximation to this quantity. $\bar{\epsilon}_p$, $\bar{\epsilon}_s$ are defined as the average error using polynomial interpolation and cubic spline interpolation, respectively, while $\epsilon_{p,max}$ and $\epsilon_{s,max}$ are the maximum errors. Referring to Table 1, it is noted that the accuracy of both interpolation schemes increases as the number of interpolation points rises, as expected. Figure 5 shows the real part of the fields associated with the reflected ray in the lit region $(s \in (18, 72))$ for the case of $M = 3$ (i.e. quadratic polynomial interpolation, and cubic splines defined over two intervals). Despite the low order of the interpolations, the agreement is almost perfect in the case of cubic splines (which essentially overlay the exact results in the top plot. This is more evident in the bottom plot, which shows the difference between the exact computation and the polynomial [red] and spline [blue] approximations). This simulation corresponds to the second row of Table 1.

We now examine the same scenario from the perspective of interpolating diffracted fields. In the case of polynomial interpolation, four distinct models are required. Two regions are identified within which to create polynomials that model diffraction from the vertical edge at $(50, 10, z)$. These regions comprise the trajectory both before and after the shadow boundary at $s = 18$.

Downloaded from https://www.cambridge.org/core. UNIVERSIDAD AUTONOMA METROPOLITANA, on 16 Nov 2026 at 02:12:28, subject to the Cambridge Core terms of use, available at https://www.cambridge.org/core/terms. https://doi.org/10.1017/S1759078726103778

Table 1. Reflection: Interpolation accuracy versus number of interpolation points

M	$\epsilon_{max,p}$	$\bar{\epsilon}_p$	$\epsilon_{max,s}$	$\bar{\epsilon}_s$
2	6.93×10^{-1}	2.88×10^{-1}	1.2×10^{-2}	3.1×10^{-3}
3	2.65×10^{-1}	1.09×10^{-1}	6.8×10^{-3}	2.2×10^{-3}
4	4.5×10^{-3}	8.4×10^{-4}	1.5×10^{-3}	3×10^{-4}
8	5.7×10^{-6}	7.6×10^{-7}	5.3×10^{-5}	7.5×10^{-6}

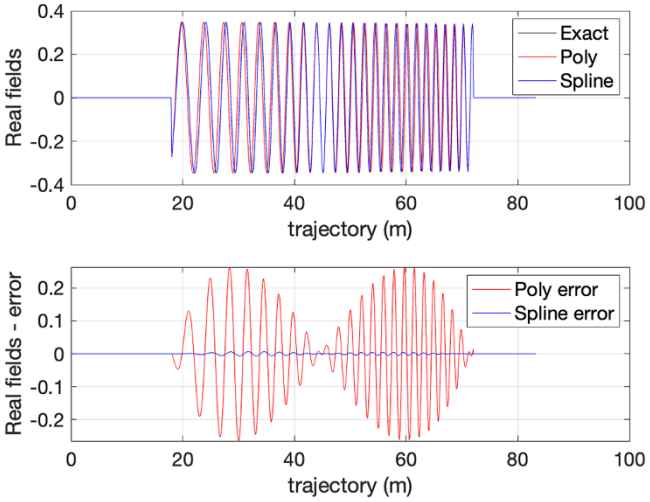


Figure 5. *Top*: Exact and approximated reflected fields along a portion of the trajectory for the validation example. Black curve is the real value of the exact z component of the electric field. Red and blue are polynomial and cubic spline interpolated approximations (the latter effectively overlaying the exact values). *Bottom*: Error between exact and interpolated fields. Red is the error associated with the polynomial, while blue is the error given by the cubic spline approximation.

Table 2. Diffraction: Interpolation accuracy versus number of interpolation points

M	$\epsilon_{max,p}$	$\bar{\epsilon}_p$	$\epsilon_{max,s}$	$\bar{\epsilon}_s$
4	9.4×10^{-2}	1.6×10^{-2}	1.1×10^{-1}	1.6×10^{-2}
6	8.2×10^{-2}	6.5×10^{-3}	3.9×10^{-2}	4.2×10^{-3}
10	2.5×10^{-1}	1.3×10^{-2}	1.7×10^{-2}	7.2×10^{-4}
16	5.9×10^{-1}	1.7×10^{-2}	1.7×10^{-2}	3.7×10^{-4}
20	3.8×10^{-1}	1.8×10^{-2}	1.7×10^{-2}	3.0×10^{-4}

Similarly, two regions are identified within which to create polynomials that model diffraction from the vertical edge at $(50, 40, z)$. These regions correspond to the portion of the trajectory before and after the shadow boundary at $s = 72$. M interpolation points are used in each of the four regions. In each case, exact data at these points is used to make a single polynomial of degree $M-1$ in this region or a cubic spline interpolation across $M-1$ subregions. In all cases, a ray trace is required for each of the M interpolation points. In the case of cubic spline interpolation, a further two ray traces are required, one at the start and end of the interpolation regions, in order to numerically estimate the derivative of the slowly varying field quantities at these end points. Hence, for this example, $4M$ ray traces are needed for polynomial interpolation along the entire trajectory while $4(M+2) = 4M+8$ ray traces are needed for cubic spline interpolation. The error is again defined

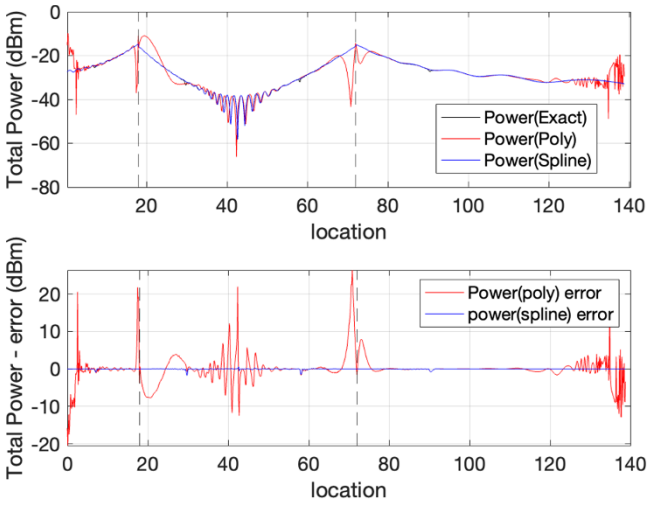


Figure 6. *Top*: Exact and approximated diffracted fields along a portion of the trajectory for the validation example. Black curve is the exact power associated with the z component of the electric field. Red and blue are $M = 20$ polynomial and cubic spline interpolated approximations (the latter effectively overlaying the exact values). *Bottom*: Error between exact and interpolated fields. Red is the error associated with the polynomial, while blue is the error given by the cubic spline approximation. Black vertical dotted lines indicate the location of the shadow boundaries.

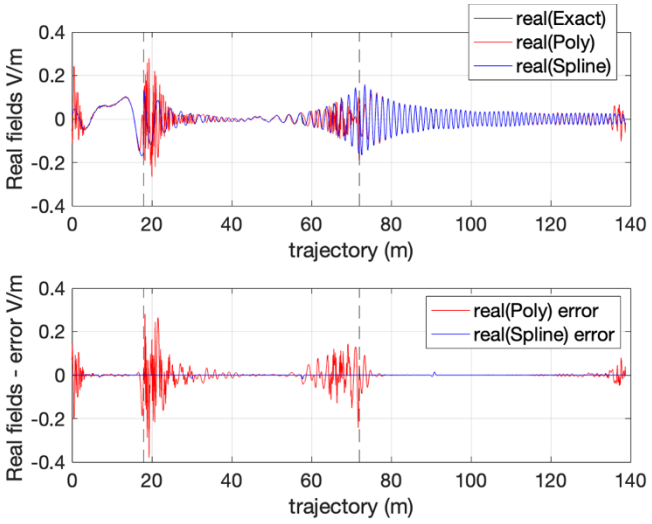


Figure 7. *Top*: Exact and approximated diffracted fields along a portion of the trajectory for the validation example. Black curve is the real value of the exact z component of the electric field. Red and blue are polynomial and cubic spline interpolated approximations (the latter effectively overlaying the exact values). *Bottom*: Error between exact and interpolated fields. Red is the error associated with the polynomial, while blue is the error given by the cubic spline approximation. The dotted vertical lines denote the position of the shadow boundaries.

as per Equation (16). Referring to Table 2 it is noted that cubic spline offers a more stable interpolation method in this instance. This is due to the relatively rapid variations of the interpolated quantities in the vicinity of the shadow boundaries. Polynomial interpolation can fit the sampled data but is subject to very rapid oscillation at intermediate points as M grows. In contrast, cubic splines offer sufficient flexibility to model the fields within each sub-domain but are low order and do not introduce instabilities at non-sampled points. This is illustrated in Figures 6 and 7, which respectively show the absolute value of the diffracted field and the

Downloaded from https://www.cambridge.org/core. UNIVERSIDAD AUTONOMA METROPOLITANA, on 16 Nov 2026 at 02:12:28, subject to the Cambridge Core terms of use, available at https://www.cambridge.org/core/terms. https://doi.org/10.1017/S1759078726103778

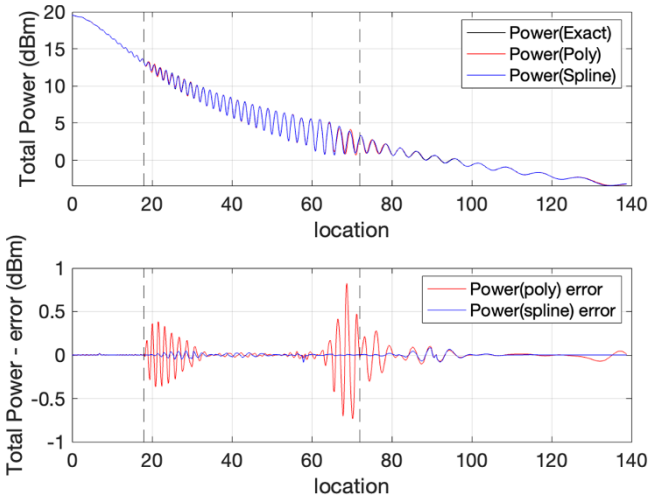


Figure 8. Total power along validation route. *Top* plot shows exact power and two interpolated approximations. *Bottom* plot shows error in polynomial approximation (red) and spline approximation (blue).

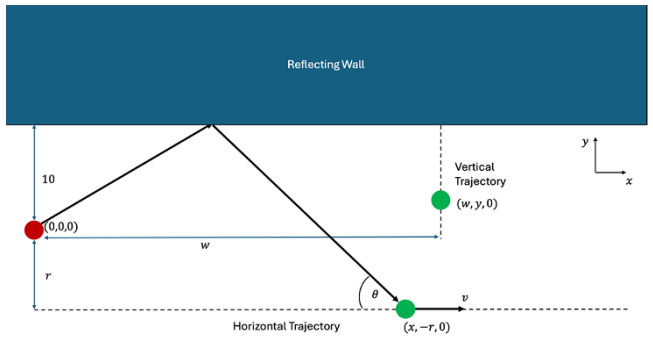


Figure 9. Geometry for error bound analysis.

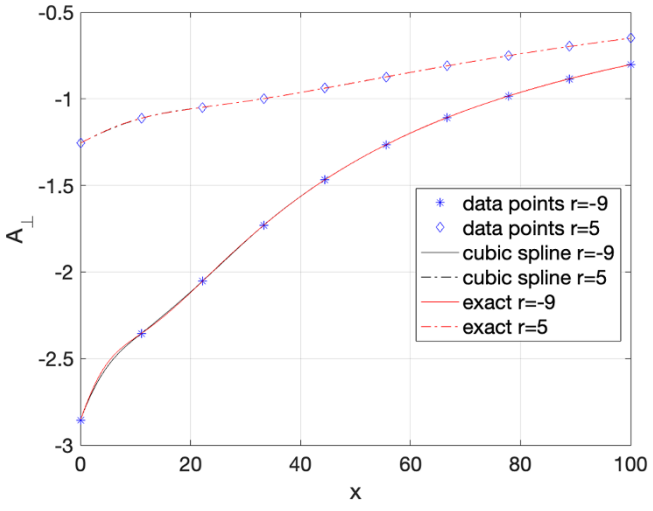


Figure 10. $A_\perp$ associated with the reflected ray computed along two horizontal trajectories from $(0, -r, 0)$ to $(100, -r, 0)$ (for $r = -9$ and $r = 5$) 10 data points are used in each case to make the cubic spline interpolated approximation.

real value of the diffracted field along the receiver trajectory for the case of $M = 16$. Note the rapid oscillations in the fields in

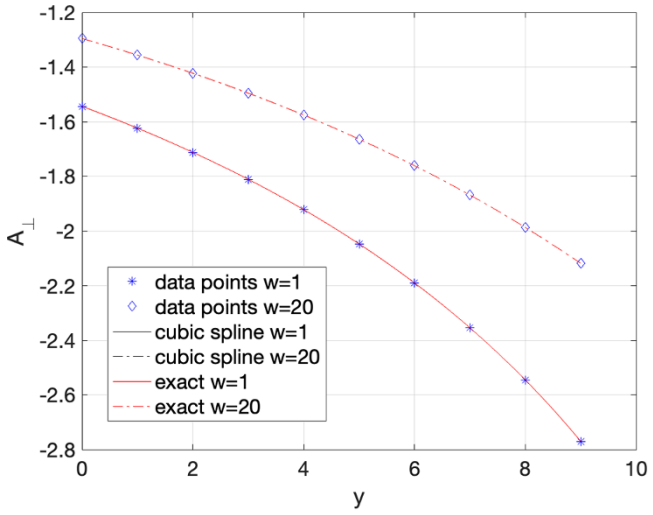


Figure 11. $A_\perp$ associated with the reflected ray computed along two vertical trajectories from $(w, 0, 0)$ to $(w, 9, 0)$. 10 data points are used in each case to make the cubic spline interpolated approximation.

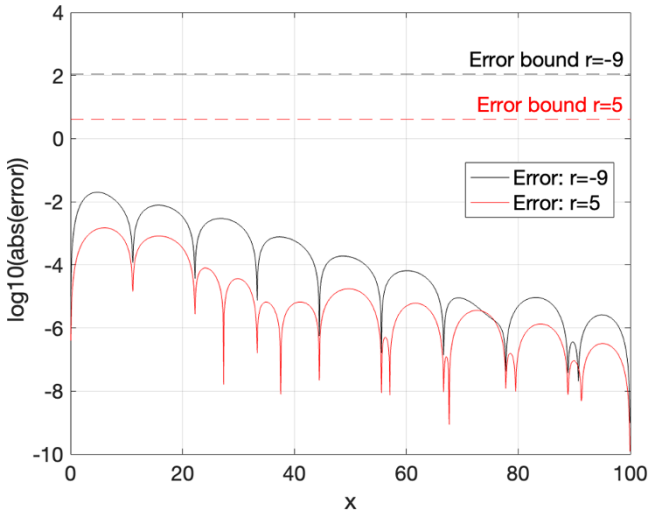


Figure 12. Error between exact and approximate values of $A_\perp$ as plotted in Figure 10. Black curve shows the error for $r = -9$, while red shows the error for $r = 5$. Error bounds (Equation (17)) included for reference.

the vicinity of the shadow boundaries when polynomial interpolation is employed. In contrast, the fields produced by cubic splines are stable throughout the region and offer excellent agreement with the exact values. Figure 7 shows the real-valued fields for this same example. Again, the cubic spline is able to accurately model the fields near the shadow boundaries as well as their phase evolution along the route.

Finally, Figure 8 shows the total fields (incident plus reflected plus diffracted rays) along the entire trajectory. Exact fields are shown along with interpolated fields for the case $M = 8$. The superior performance of the cubic spline interpolation is evident in the lower plot, which shows the error in the approximated fields along the route. The cubic spline interpolation essentially overlays the exact result.

Downloaded from https://www.cambridge.org/core. UNIVERSIDAD AUTONOMA METROPOLITANA, on 16 Nov 2026 at 02:12:28, subject to the Cambridge Core terms of use, available at https://www.cambridge.org/core/terms. https://doi.org/10.1017/S1759078726103778

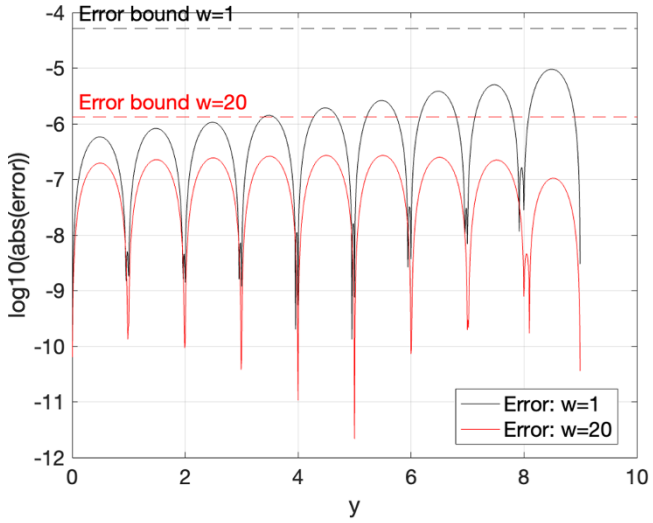


Figure 13. Error between exact and approximate values of $A_\perp$ as plotted in Figure 11. Black curve shows error for $w = 1$ while red shows error for $w = 20$. Error bounds (Equation (17)) included for reference.

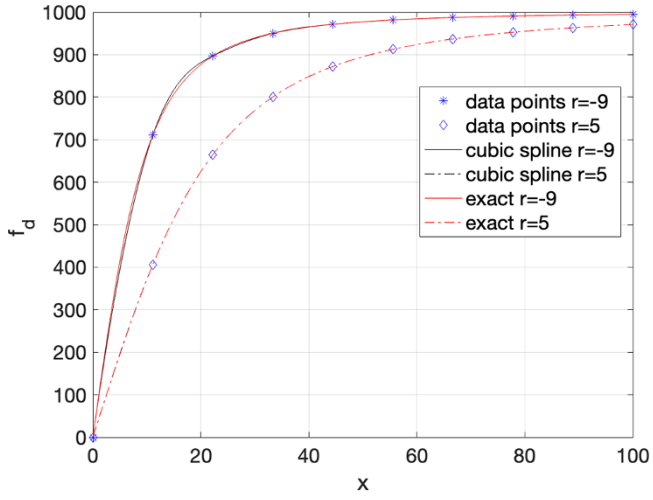


Figure 14. Doppler shift experienced by receiver traveling at 50 ms^{-1} along horizontal trajectories depicted in Figure 9. Cubic spline interpolation based on 10 sampled values along the trajectory.

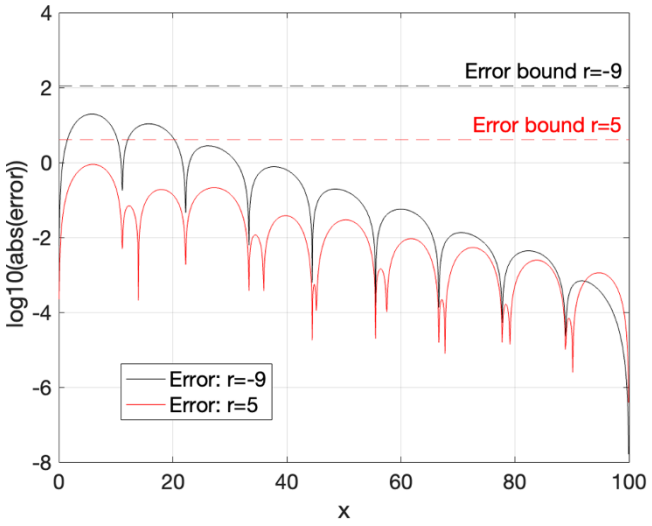


Figure 15. Errors and error bounds for Doppler shift example.

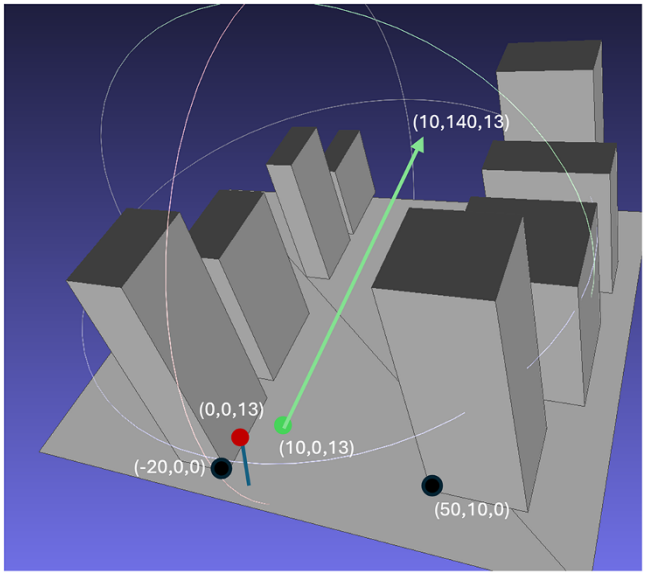


Figure 16. Street-canyon geometry.

Error bounds and sampling requirements

The use of cubic splines allows a rudimentary level of error analysis to be performed. In particular, it is shown in [16] that if a function f is approximated using a cubic spline p based on equispaced samples a distance h apart, the maximum error is bounded as follows

$$\|f - p\|_\infty \leq C_0 \|f^{(4)}\|_\infty h^4 \tag{17}$$

with $C_0 = \frac{5}{384}$ and $f^{(4)}$ the fourth derivative of f. The validity of this bound is explored below.

Consider the situation in Figure 9. A vertical dipole is placed at $(0, 0, 0)$, $10m$ from a reflecting wall ($\epsilon_r = 4$). It radiates at $6GHz$. The fields associated with the reflected ray will be examined along horizontal (parallel to the wall) and vertical (perpendicular to the wall) trajectories. The horizontal trajectory runs from $(0, -r, 0)$ to $(100, -r, 0)$, while the vertical trajectory is shorter and runs from $(w, 0, 0)$ to $(w, 9, 0)$. In each case, 10 sample points are chosen along the trajectory in order to create data to make the approximation. This means that the sampling distance h is equal to 11.11 m and 1 m in the horizontal and vertical trajectories, respectively.

Figures 10 and 11 show $A_\perp$ and its cubic spline approximation for both the horizontal and vertical trajectories, respectively. A high level of agreement can be noted, with the exact and interpolated values essentially overlapping. A better sense of the accuracy can be obtained from Figures 12 and 13, which show the error between the exact $A_\perp$ and its interpolated value (on a log scale) along the horizontal and vertical trajectories, respectively. The error bound (Equation (17)) is included in each case for reference. It is seen that the error is indeed bounded by the theoretical bound in each case. As can perhaps be expected, the error is largest for points where the reflection coefficient is changing most rapidly (i.e. in Figure 12 when $r = -9$ and the points are near the wall). Note that the fourth derivative information, $\|f^{(4)}\|_\infty$, needed to compute the bound was explicitly computed for this purely illustrative example.

Downloaded from https://www.cambridge.org/core. UNIVERSIDAD AUTONOMA METROPOLITANA, on 16 Nov 2026 at 02:12:28, subject to the Cambridge Core terms of use, available at https://www.cambridge.org/core/terms. https://doi.org/10.1017/S1759078726103778

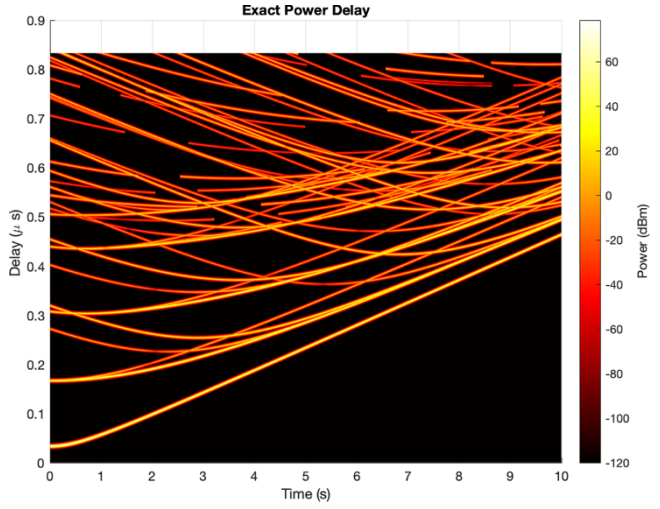


Figure 17. Exact time-varying power delays along receiver route.

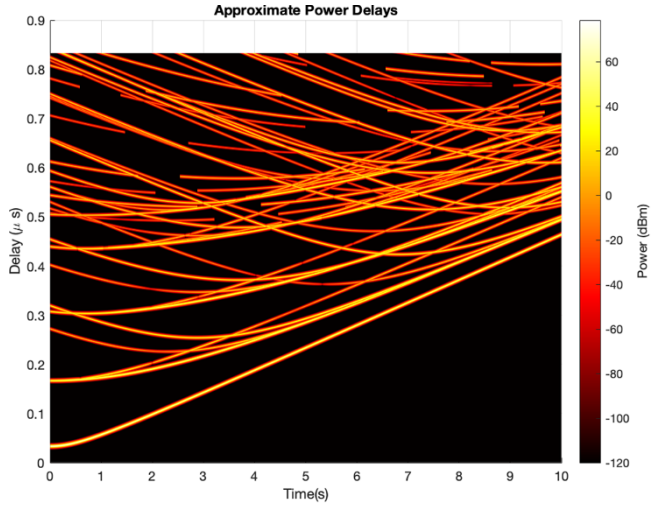


Figure 18. Approximate time-varying power delays along the receiver route using cubic spline interpolation.

This analysis can be applied to other physical quantities associated with an interpolated ray. Assuming a receiver moving at v ms^{-1} along the horizontal trajectory depicted in Figure 9, one can compute the Doppler shift associated with the reflected ray as

$$f_D = \frac{v}{\lambda}\cos\theta \tag{18}$$

Figure 14 shows the Doppler shift associated with this multipath component, computed exactly and one based on cubic spline interpolation for the case where $v = 50\text{ms}^{-1}$. The errors are shown in Figure 15 along with the error bounds.

It can be seen that the bound given by Equation (17) represents a usefully tight bound on the error. In particular, Equation (17) can be rearranged to express the sampling spacing required to achieve a desired accuracy. In particular, if the error is to be no greater than ϵ along a path, then h must satisfy

$$h \leq \left(\frac{\epsilon}{C_0\|f^{(4)}\|_\infty}\right)^{\frac{1}{4}} \tag{19}$$

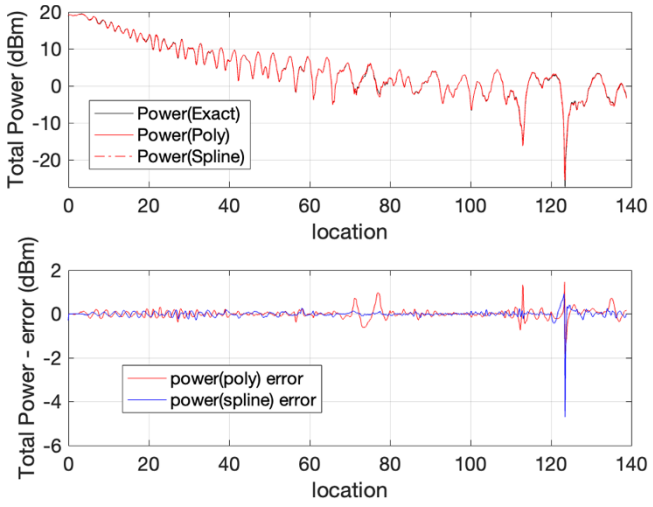


Figure 19. *Top*: Total narrowband power along trajectory indicated in Figure 16. *Bottom*: Error between interpolated and exact power.

Table 3. Channel metric errors for various values of M

M	ϵ_{max} (dBm)	ϵ_{avg} (dBm)	ϵ_{NMSE}	ϵ_τ (ns)
6	4.703	7.69×10^{-2}	5×10^{-4}	1.07×10^{-1}
8	1.284	4.59×10^{-2}	1×10^{-4}	6.7×10^{-2}
10	6.96×10^{-1}	2.8×10^{-2}	5.9×10^{-5}	5.4×10^{-2}

Clearly, the slower the variation of the function (as measured by the maximum value of its fourth derivative), the fewer interpolation points are necessary to achieve a specified accuracy. This bound is thus a useful starting point to develop practical guidelines on the level of field sampling necessary to reliably implement the interpolation. However, it does require knowledge of the fourth derivative of the quantity to be approximated. This was computed exactly for these illustrative examples but will need to be reliably estimated if this analysis is to support practical implementation. This will be a focus of future work.

Results

In this section, the performance of the interpolation schemes is examined in the context of propagation in a street canyon comprising eight buildings (Figure 16) and a transmitter radiating at 300 MHz. A receiver travels for 10 s at a speed of 50 km/h along the indicated linear route, covering a distance of total of just under 140 m. It enters and exits multiple lit regions corresponding to multiple higher-order rays as it travels. The field is calculated at 1200 locations along the trajectory, and up to 2 reflections/diffractions were allowed, using the DCU in-house ray tracer previously developed in the context of references [6], [7], and [11]. The reference solution involved an exact ray trace at each location and required the computation of 62,183 rays, which took 590 s with an Apple M4 processor. To create the approximate model, suitable M was set to 6 for each lit region. Fields were approximated using the concepts in Sections "Interpolation of reflected rays" and "Interpolation of diffracted rays." For polynomial interpolation, this meant that fifth-order polynomials were created. This required the explicit computation of 3858 rays, and the total process took 3.5 s, a saving of 99.5%. For cubic spline interpolation, this meant that

Downloaded from https://www.cambridge.org/core. UNIVERSIDAD AUTONOMA METROPOLITANA, on 16 Nov 2026 at 02:12:28, subject to the Cambridge Core terms of use, available at https://www.cambridge.org/core/terms. https://doi.org/10.1017/S1759078726103778

each lit region was divided into 5 sub-domains. This required the explicit calculation of 5144 rays and took 4.8 s, a saving of roughly 99.2%.

Figure 17 depicts how the power delay varies with time (horizontal axis) as the receiver moves along the trajectory. It was computed using exact RT. Each curve represents the contribution caused by a single ray (multipath component) and its color denotes the power associated with that component. The lowest curve denotes the incident field via direct line of sight, while all other curves represent some higher-order combination of reflected/diffracted rays. Figure 18 shows the same information computed using the cubic spline interpolation. Finally, the total narrow band fields along the route are depicted in Figure 19. Both interpolated results show excellent agreement with the exact values.

To examine the effect of interpolation accuracy on channel-level metrics, we computed various KPI for different values of M. If p_i is the exact received power at location i and $\tilde{p}_i$ is the interpolated value, we define the maximum, average, and normalized mean square errors as

$$\begin{aligned} \epsilon_{max} &= \max_i |p_i - \tilde{p}_i| \\ \epsilon_{avg} &= \frac{1}{N}\sum_{i=1}^{N} |p_i - \tilde{p}_i| \\ \epsilon_{NMS} &= \frac{\sum_{i=1}^{N} (p_i - \tilde{p}_i)^2}{\sum_{i=1}^{N} p_i^2} \end{aligned}$$

We also compute the RMS delay spread τ_i at each location as well as its value based on cubic spline interpolation $\tilde{\tau}_i$. We define the average RMS delay spread error as

$$\epsilon_\tau = \frac{1}{N}\sum_{i=1}^{N} |\tau_i - \tilde{\tau}_i|$$

Table 3 shows how these values vary for the trajectory in Figure 16 for various values of M using cubic spline interpolation.

Conclusion

This paper proposes a novel approximate method to compute reflected and diffracted fields along the trajectory of a moving receiver. The rapidly oscillating field associated with each ray is factorized into a product of terms, each of which can be modeled using a low-degree interpolation. Both polynomial interpolation and cubic spline interpolation are employed, and both are shown to be effective in accurately modeling field behavior within the corresponding lit region. However, cubic spline interpolation is shown to be more stable as the degree of interpolation is raised in order to increase accuracy. Results demonstrate good agreement for examples involving a single reflecting face and a street canyon. Results were provided showing excellent agreement for both field strength and channel delay. Future work will extend the method to the case of a moving TX/RX pair. In addition, we intend to extend the ideas to the problem of diffuse scattering, whereby field contributions are collected from a grid of patches on each face. The geometric quantities underpinning diffuse scattering vary slowly, thereby making it a candidate for the approach outlined in this paper.

Competing interests. The authors declare none.

References

1. **Liu F, Cui Y, Masouros C, Xu J, Han TX, Eldar YC and Buzzi S** (2022) Integrated sensing and communications: Toward dual-functional wireless networks for 6G and beyond. *IEEE Journal on Selected Areas in Communications* **40**(6), 1728–1767.
2. **Schiller M, A Knoll, M Mocker and T Eibert** (2015). GPU Accelerated Eay Launching for High-Fidelity Virtual Test Drives of VANET Applications. In *2015 International Conference on High Performance Computing & Simulation (HPCS)*, Amsterdam, Netherlands, pp. 262–268.
3. **Fan W, Carton I, Kyösti P and Pedersen GF** (2016) Emulating ray-tracing channels in multiprobe anechoic chamber setups for virtual drive testing. *IEEE Transactions on Antennas and Propagation* **64**(2), 730–739.
4. **Mbugua AW, Y Chen, L Raschkowski, L Thiele, S Jaeckel and W Fan** (2021) Review on ray tracing channel simulation accuracy in sub-6 GHz outdoor deployment scenarios. *IEEE Open J. Antennas Propag* **2**, 22–37. https://doi.org/10.1109/OJAP.2020.3041953
5. **Wang R and D Manocha** (2022) Dynamic Coherence-Based EM Ray Tracing Simulations in Vehicular Environments. In *2022 IEEE 95th Vehicular Technology Conference: (VTC2022-Spring)*, Helsinki, Finland, pp. 1–7.
6. **Hussain S and Brennan C** (2019) Efficient preprocessed ray tracing for 5G mobile transmitter scenarios in urban microcellular environments. *IEEE Transactions on Antennas and Propagation* **67**(5), 3323–3333.
7. **Hussain S and Brennan C** (2023) An efficient ray validation technique for ray-tracing in urban microcellular environments. *IEEE Antennas and Wireless Propagation Letters* **22**(6), 1401–1405.
8. **Bilibashi D, EM Vitucci and V Degli-Esposti** 2020 Dynamic Ray Tracing: Introduction and Concept. in *Proc. 14th Eur. Conf. Antennas Propag (EuCAP)*, Copenhagen, Denmark.
9. **Bilibashi D, Vitucci EM and Degli-Esposti V** (2023) On dynamic ray tracing and anticipative channel prediction for dynamic environments. *IEEE Transactions on Antennas and Propagation* **71**(6), 5335–5348.
10. **Quatresooz F, Demey S and Oestges C** (2021) Tracking of interaction points for improved dynamic ray tracing. *IEEE Transactions on Antennas and Propagation* **70**(7), 6291–6301.
11. **Hussain S and Brennan C** (2017) An efficient ray tracing method for propagation prediction along a mobile route in urban environments. *Radio Science* **52**(7), 862–873.
12. **Nuckelt J, M Schack and T Kürner** 2015 Geometry-Based Path Interpolation for Rapid Ray-Optical Modeling of Vehicular Channels. In *Proc. 9th Eur. Conf. Antennas Propag (EuCAP)*, Lisbon, Portugal, pp. 1–5.
13. **Zentner R and AK Mucalo** (2013) Ray Tracing Interpolation for Continuous Modeling of Double Directional Radio Channel. In *Proc. Eurocon*, Zagreb, Croatia, pp. 212–217.
14. **Brennan C, AW Mbugua, Y Chen and S Hussain** (2025) Interpolation of Reflected and Diffracted Rays for Accelerated Ray Tracing Simulations. In *2025 19th European Conference on Antennas and Propagation (EUCAP25)*, Stockholm, Sweden.
15. **Balanis CA** (2012) *Advanced engineering electromagnetics*, 2nd edn. Wiley, pp. 800–808.
16. **Hall CA and Meyer W** (1976) Optimal error bounds for cubic spline interpolation. *Journal of Approximation Theory* **16**(2), 105–122. Available at: https://www.sciencedirect.com/science/article/pii/002190457690040X

Downloaded from https://www.cambridge.org/core. UNIVERSIDAD AUTONOMA METROPOLITANA, on 16 Nov 2026 at 02:12:28, subject to the Cambridge Core terms of use, available at https://www.cambridge.org/core/terms. https://doi.org/10.1017/S1759078726103778



Conor Brennan received a B.A. (Mod) in Mathematics and a PhD from Dublin University (Trinity College) in 1994 and 1998, respectively. He joined the School of Electronic Engineering, Dublin City University in 2003, where he is a Professor. He has served as the Irish Representative on multiple COST Actions in the area of wireless communications and is a teacher on the European School of Antennas and Propagation. In 2026, he was the General Chair of the European Conference on Antennas and Propagation (EuCAP26). He has authored more than 100 peer-reviewed publications in international journals and conference proceedings. His current research interests include wireless communications and computational methods for electromagnetic wave scattering and propagation. Dr. Brennan is an Associate Editor of IEEE Transactions on Antennas and Propagation.



Allan Wainaina Mbugua received the B.Sc. degree in telecommunication and information engineering from the Jomo Kenyatta University of Agriculture and Technology, Juja, Kenya, in 2014; the M.Sc. degree in telecommunications engineering from the University of Cassino and Southern Lazio, Cassino, Italy, in 2018; and the Ph.D. degree from Aalborg University, Aalborg, Denmark, in 2023. He is currently working as a Senior Engineer with Huawei Technologies Duesseldorf GmbH, Munich, Germany. His current research interests include radio channel sounding, radio channel simulation, and radio channel emulation.



Dr. Yun Chen received the B.Sc. from the University of Duisburg-Essen, Germany, in 2006, the M.Sc. degree from the University of Duisburg-Essen, Germany, in 2008, and the Ph.D. degree from the University of Duisburg-Essen, Germany, in 2012. He was with Rohde & Schwarz and Fraunhofer research society in Munich, Germany, and is currently working as a team manager with Huawei Technologies Duesseldorf GmbH, Munich, Germany, with a research focus on 5G, WiFi, and smart home systems testing and simulations.



Sajjad Hussain received the B.Sc. degree in electrical engineering from the University of Engineering and Technology at Taxila, Taxila, Pakistan, in 2006, the M.Sc. degree in telecommunications engineering from the University of Liverpool, Liverpool, UK, in 2008, and the Ph.D. degree in electronic engineering from Dublin City University, Dublin, Ireland, in 2017. From 2009 to 2013, he was a Technical and Test Engineer with Vodafone Automotive Ltd., Manchester, UK. He is currently an Assistant Professor with the School of Electrical Engineering and Computer Sciences, National University of Sciences and Technology, Islamabad, Pakistan. His research interests include radio channel modeling for future radio networks using RT and machine learning.

Downloaded from https://www.cambridge.org/core. UNIVERSIDAD AUTONOMA METROPOLITANA, on 16 Nov 2026 at 02:12:28, subject to the Cambridge Core terms of use, available at https://www.cambridge.org/core/terms. https://doi.org/10.1017/S1759078726103778